Electronic Supplementary Material (ESI) for Chemical Communications.
This journal is © The Royal Society of Chemistry 2019

Supporting Information

Confinement Growth of 2D MoS_2 Nanosheets in N-doped Pearl Necklace-like Structured Carbon Nanofibers with Boosted Lithium and Sodium Storage Performance

Huayu Wu, Xiue Zhang, Qianhui Wu, Yue Han, Xiaoyu Wu, Penglei Ji, Min Zhou, Guowang Diao, Ming Chen*

School of Chemistry and Chemical Engineering, Yangzhou University, Yangzhou 225002, P. R. China

Experimental section

Materials

Polyacrylonitrile (PAN, M_w=150000) was purchased from Aladdin. N-dimethyformatide (DMF), $Na_2MoO_4 \cdot 2H_2O$, thiourea, resorcinol, formaldehyde, $NH_3 \cdot H_2O$, ethanol, NaOH and polyvinylidene difluoride (PVDF) are analytical grade and purchased from Shanghai Chemical Corp. The electrolyte solution with 1 M $LiPF_6$/ethylene carbonate (EC)/diethyl carbonate (DMC)/ethyl methyl carbonate (EMC) (1: 1: 1 by volume) and 1 M $NaClO_4$ in a mixture of ethylene carbonate (EC) and propylene carbonate (PC) (1:1 in volume) with 5 wt % fluoroethylene carbonate (FEC) were supplied by Guangzhou Tinci Materials Technology Co., Ltd. Other

---

* Corresponding authors.
E-mail address: chenming@yzu.edu.cn (M. Chen)

chemicals and solvents are reagent grade and commercially available. Deionized water was used for all experiments.

Synthesis of SiO_2@SiO_2/RF core-shell structured nanospheres

Tetraethyl orthosilicate (TEOS) and resorcinol-formaldehyde (RF) oligomers were polymerized on SiO_2 core particles to form the SiO_2@SiO_2/RF core-shell structured nanospheres. In a typical synthesis of SiO_2@SiO_2/RF, 3.46 mL TEOS was added to the solution containing 70 mL ethanol, 10 mL H_2O, and 3 mL ammonia solution (25 wt%) under vigorous stirring at room temperature. After 20 min, 0.4 g resorcinol and 0.56 mL formaldehyde (37 wt %) were added to the solution and the system was kept under vigorous stirring for 24 h at room temperature. The precipitates were separated by centrifugation, washed with deionized water and ethanol, and then dried at 60 °C overnight.

Synthesis of pearl necklace-like structured carbon nanofibers (PNL CNFs)

0.75 g of polyacrylonitrile (PAN, M_W=150000) was dissolved in 10 mL of N, N-dimethylformamide (DMF) with strong magnetic stirring for 6 h. The SiO_2@SiO_2/RF core-shell structured nanospheres were synthesized according to our previously reported (the more detail in Supporting Information). Then 0.3 g SiO_2@SiO_2/RF nanospheres were added into the DMF solution of PAN. The above-mentioned mixture solution was stirred for 10 h under room temperature. The obtained spinning solution was loaded into the syringe with a 23-gauge needle tip. For the electrospinning, the flow rate of the solution was 0.1 mL h^{-1}, the voltage was 15 kV and the distance between the tip and the collector was 15 cm. After electrospinning process, the as-prepared SiO_2@SiO_2/RF@PAN nanofibers were heated at 700 ^{o}C for 2h at a heating rate of 2 ^{o}C min^{-1} under Ar atmosphere. The novel pearl necklace-like structured SiO_2/C@CNFs composite nanofibers were obtained. Finally, the pearl necklace-like structured carbon nanofibers (PNL CNFs) were obtained by removing silica using sodium hydroxide (NaOH, 1 M).

Synthesis of amber necklace-like structure MoS_2@CNFs (ANL MoS_2@CNFs)

0.5 g $Na_2MoO_4 \cdot 2H_2O$ and 1.0 g $CS(NH_2)_2$ were dissolved into 30 mL deionized water to form a transparent solution under ultrasonic dispersion for 30 min, followed by dispersing 100 mg PNL CNFs to the solution. After ultrasonic dispersion for 50 min, the black solution was transferred to a 60 mL Teflon-lined stainless-steel autoclave. The autoclave was then heated in an air-flow electric oven at 200 °C for 4 h. After that, the autoclave was cooled to room temperature. The solution was transferred out for centrifugation. The final products were collected and washed six times with deionized water and ethanol before being dried at 60 °C in vacuum overnight. Then the product was calcined in a tube furnace at 800 °C for 2h under Ar atmosphere, to obtain amber necklace-like structure MoS_2@CNFs. In addition, all characterization and electrochemical tests are displayed in Supporting Information.

Materials Characterization

Field-emission scanning electron microscopy (FESEM) was carried out with Hitachi S-4800 (Japan). Transmission Electron Microscopy (TEM) was conducted on Philips TECNAI-12 instrument. High-resolution TEM (HRTEM) and high-angle annular dark-field scanning transmission electron microscopy (HAADF-STEM) were performed on FEI Tecnai G2 F30 STWIN (USA) operating at 300 kV. X-ray diffraction (XRD) data were obtained with a graphite monochromator and Cu Kα radiation (λ= 0.1541 nm) on D8 advance superspeed powder diffractometer (Bruker). Raman spectra were carried out on Renishaw via Raman spectroscopy. X-ray photoelectron spectroscopy (XPS) were conducted by Thermo Escalab 250 system using Al Ka radiation (hv = 1486.6 eV). The pressure of test chamber was maintained below 2×10^{-9} Torr during spectral acquisition. Thermogravimetry analysis (TGA) (Pyris 1 TGA, PerkinElmer, USA) was performed under air atmosphere from room temperature to 800 ^{o}C at a heating rate of 10 ^{o}C min^{-1}. Surface areas and pore size distributions were recorded by BET technique in an automated surface area and porosity analyzer (ASAP 2020, HD88) at -196 ^{o}C after samples being dried at 100 ^{o}C for 4 h.

Electrochemical Tests

Anode electrodes were prepared by mixing the amber necklace-like structure MoS_2@CNFs (80%) with 10 % acetylene black as a conductive material, and 10 % polyvinylidene difluoride (PVDF) binder dissolved in N-methyl-2-pyrrolidinone (NMP). Then, the slurries were cast onto a copper foil current collector. After coating, the electrodes were dried at 80 °C for 10 h to remove the solvent before pressing. The electrodes were punched in the form of disks and then vacuum-dried at 120 °C for 12 h. And then the button cells (CR 2032 coin-type cell) were assembled with metallic lithium and sodium as the counter/reference electrode, 1 M $LiPF_6$ in EC/DMC/EMC (1:1:1 by volume) and 1 M $NaClO_4$ in EC/PC (1:1 in volume)/5wt% FEC as electrolyte, and Celgard 2400 polypropylene as separator in a high-purity argon-filled glovebox (Vacuum Atmospheres Co., Ltd).

Cyclic voltammetry (CV) measurements were performed using an electrochemical workstation (CHI660 E, Chenghua, CHN) at a scan rate of 0.1 mV s^{-1} between 0 and 3.0 V. Electrochemical impedance spectroscopic (EIS) experiments were performed with Autolab Electrochemical Analyzer (Ecochemie, Netherlands). Galvanostatic charge (lithium insertion) and discharge (lithium extraction) cycling of the cells were carried out using a battery test system (CT-3008W, Xinwei, CHN) at the various current densities between 0.005 and 3 V to determine ratio performance, and to evaluate cycle stability at the current density of 1 A g^{-1}.

Supplementary Figures captions

Figure S1 TEM images of (a, b) the size of 260 nm SiO_2@SiO_2/RF nanospheres.

Figure S2 SEM images of (a, b) SiO_2/C@CNFs, (c, d) PNL CNFs, (e, f) PAN nanofibers and (g, h) ANL MoS_2@CNFs.

Figure S3 TGA curves of the ANL MoS_2@CNFs and pure MoS_2.

Figure S4 Schematic illustration of the formation of SG MoS_2@CNFs.

Figure S5 TEM images of (a, b) the SG MoS_2@CNFs.

Figure S6 (a) BET nitrogen adsorption and desorption isotherms and (b) pore size distribution of the ANL MoS_2@CNFs.

Figure S7 BET nitrogen adsorption and desorption isotherms of the SG MoS_2@CNFs.

Figure S8 TEM images of (a, b) the pure MoS_2.

Figure S9 XPS of ANL MoS_2@CNFs survey spectrum.

Figure S10 TEM images at different reaction time (a, b) 2 h, (c, d) 4 h and (e, f) 6 h. (g-h) the sample obtained at hydrothermal reaction condition: 1 g $Na_2MoO_4 \cdot 2H_2O$, 2.0 g $CS(NH_2)_2$ and 30 mL deionized water.

Figure S11 (a) CV and (b) charge/discharge voltage profiles of pure MoS_2 for LIBs.

Figure S12 Cycling performance for LIBs of PNL CNFs after 500 cycles at 1A g^{-1}.

Figure S13 Cycling performance for LIBs of PNL CNFs at various current densities (0.1 to 10 A g^{-1}).

Figure S14 (a) Nyquist plots of ANL MoS_2@CNFs, SG MoS_2@CNFs and pure MoS_2; Nyquist plots of (b) ANL MoS_2@CNFs and (c) SG MoS_2@CNFs after 100 and 300 cycles.

Figure S15 Graph for LIBs of the *Z′* plotted against $\omega^{-1/2}$ at low frequency region.

Figure S16 Electrochemical performance for SIBs. CV and charge/discharge voltage profiles of (a, c) ANL MoS_2@CNFs, (b, d) SG MoS_2@CNFs.

Figure S17 Cycling performance of (a) ANL MoS_2@CNFs at 1, 0.5, 0.1 A g^{-1} and Coulombic efficiency of ANL MoS_2@CNFs at 0.1 A g^{-1}. (b) Cycling performances, (c) rate performances, (d) Nyquist plots of different electrode materials.

Figure S18 Cycling performance for SIBs of PNL CNFs after 100 cycles at 1 A g^{-1}.

Figure S19 Rate performance for SIBs of PNL CNFs and pure MoS_2 at various current densities.

Figure S20 Graph for SIBs of the *Z′* plotted against $\omega^{-1/2}$ at low frequency region.

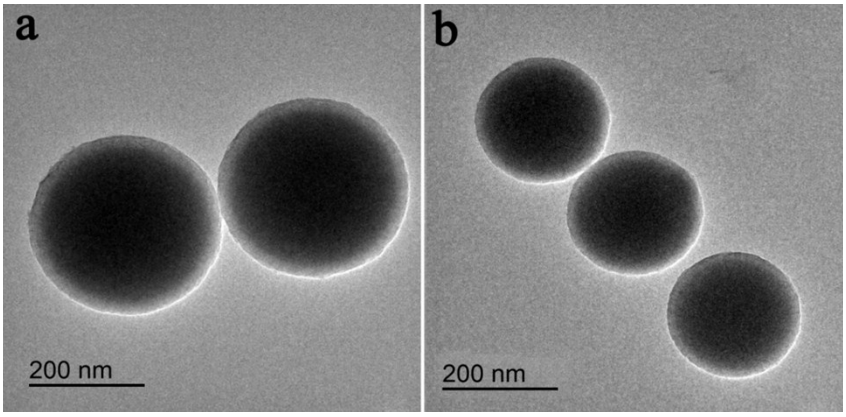

Figure S1 TEM images of (a, b) the size of 260 nm $SiO_2@SiO_2/RF$ nanospheres.

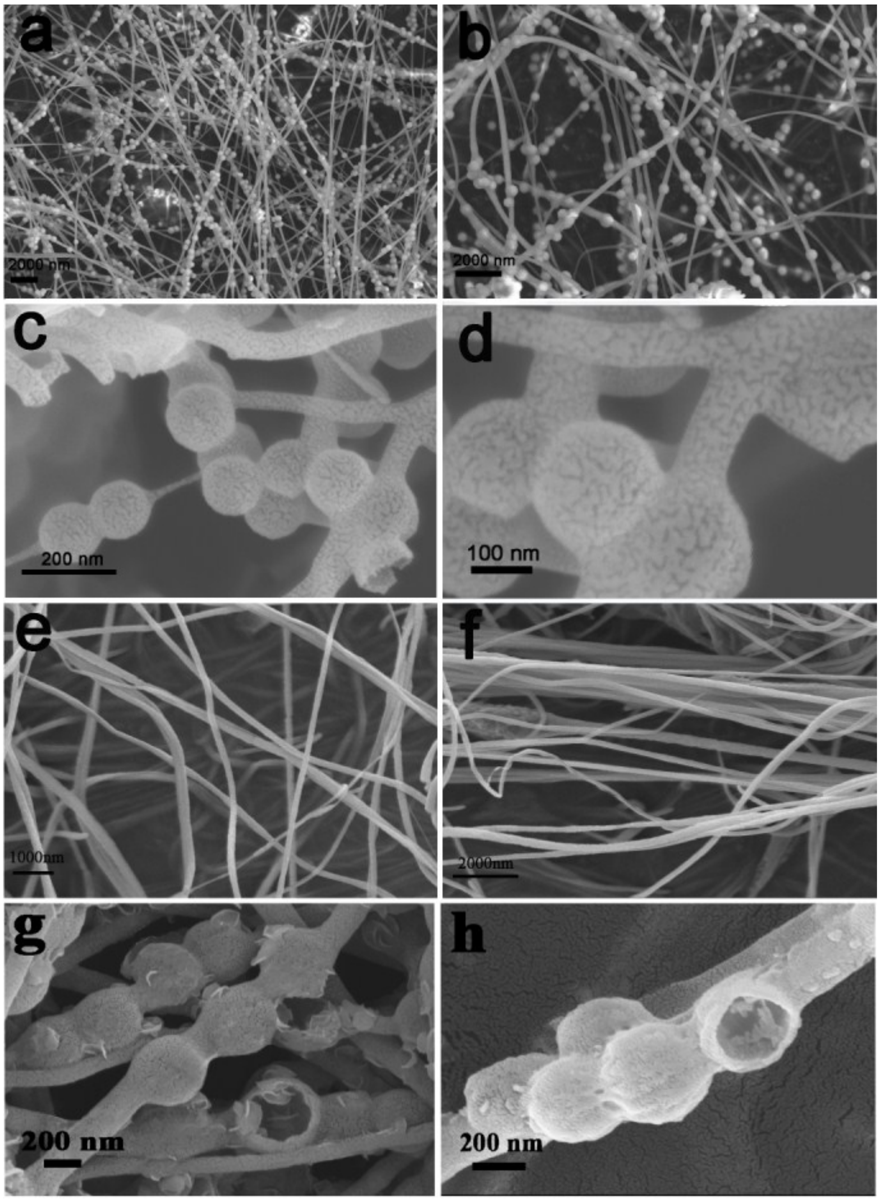

Figure S2 SEM images of (a, b) $SiO_2/C@CNFs$, (c, d) PNL CNFs, (e, f) PAN nanofibers and (g, h) ANL $MoS_2@CNFs$.

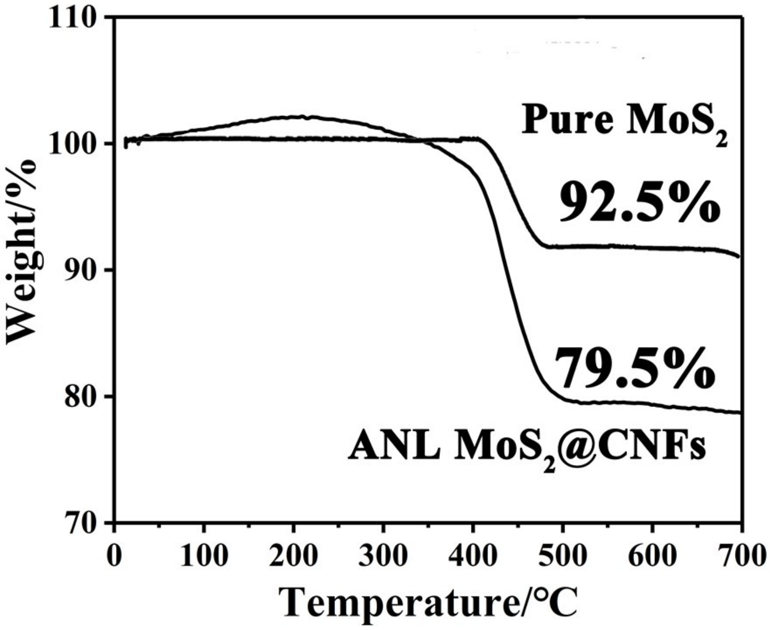

Figure S3 TGA curve of the ANL MoS$_2$@CNFs and pure MoS$_2$.

Under air atmosphere, the MoS$_2$ undergoes a weight loss owing to the oxidative reaction of MoS$_2$ to MoO$_3$. From Equation (1) and (2), we can obtain the percentage content of MoS$_2$ in the amber necklace-like nanofibers is 88.3%.

$MoS_2 + O_2 \rightarrow MoO_3 + SO_2$ (g)

The initial quality of MoS$_2$ is m_1, the initial quality of PNL CNFs is m_2.

Final residual solid is MoO$_3$, and the quality of MoO$_3$ is m_3.

MoO_3 (wt%)= $m_3/(m_1+m_2)\times 100\%$= percentage content of final residual solid (1)

(m_3/ MoO$_3$ molecular weight) = (m_1/ MoS$_2$ molecular weight) (2)

From Equation (1) and (2), we can obtain the percentage content of MoS$_2$ in the amber necklace-like nanofibers

$$MoS_2\ (wt\%) = m_1/(m_1+m_2)\times 100\% \qquad (3)$$

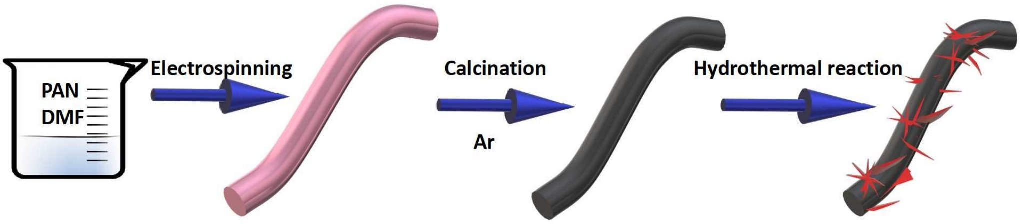

Figure S4 Schematic illustration of the formation of SG MoS_2@CNFs.

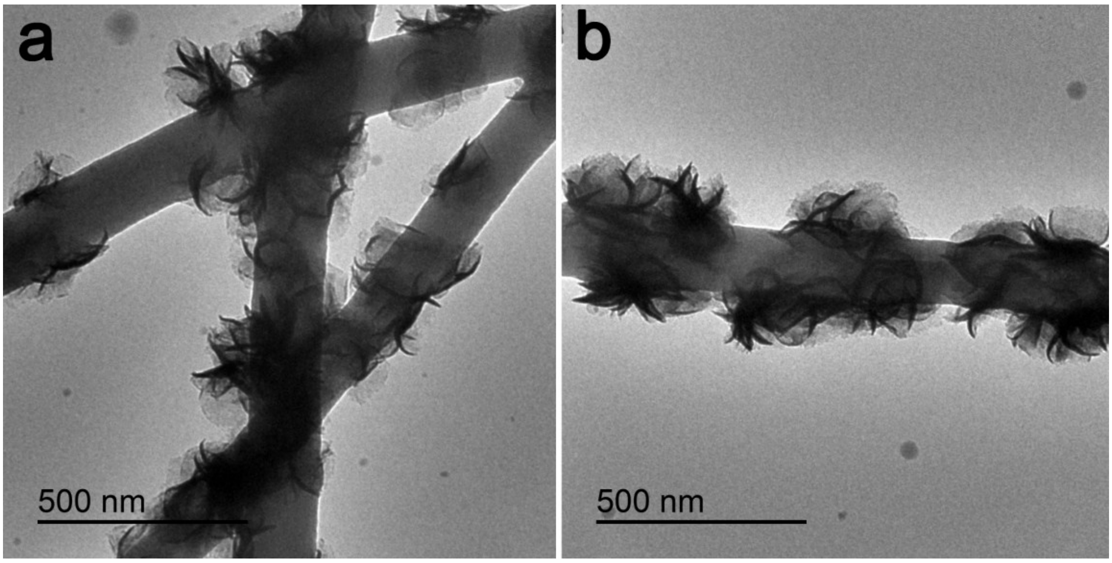

Figure S5 TEM images of (a, b) the SG MoS_2@CNFs.

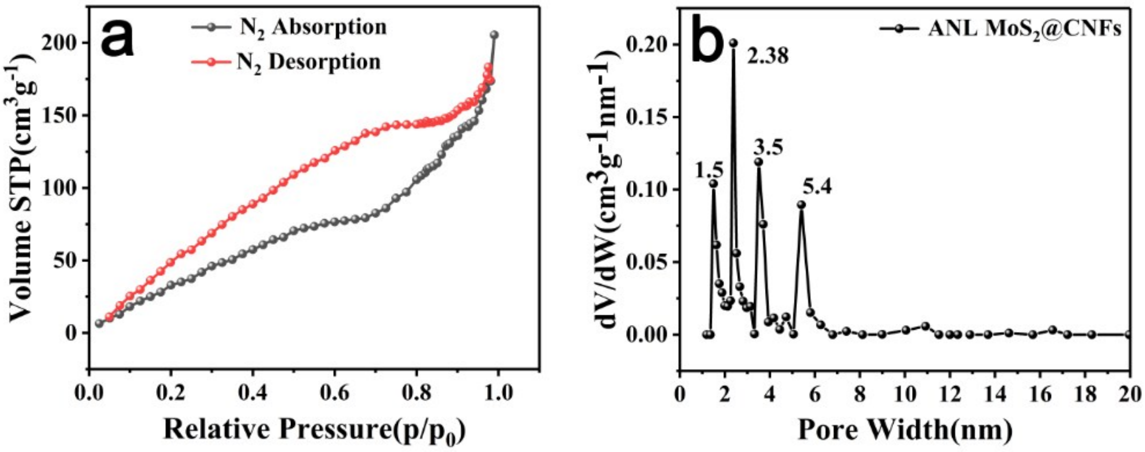

Figure S6 (a) BET nitrogen adsorption and desorption isotherms and (b) pore size distribution of the ANL MoS_2@CNFs.

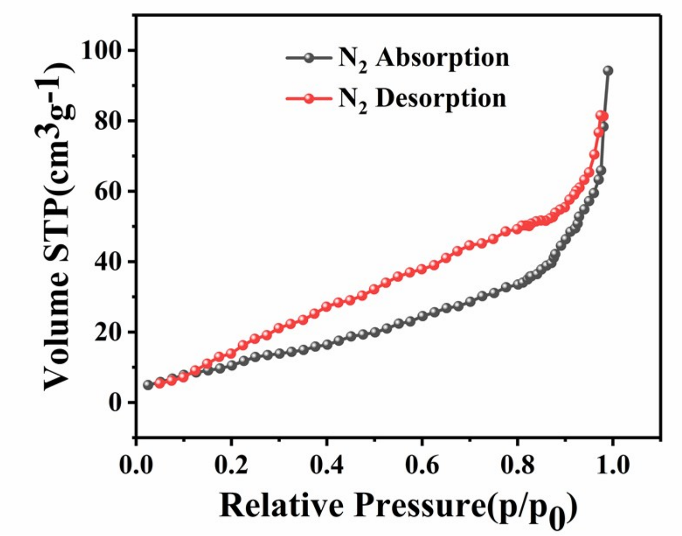

Figure S7 BET nitrogen adsorption and desorption isotherms of the SG MoS_2@CNFs.

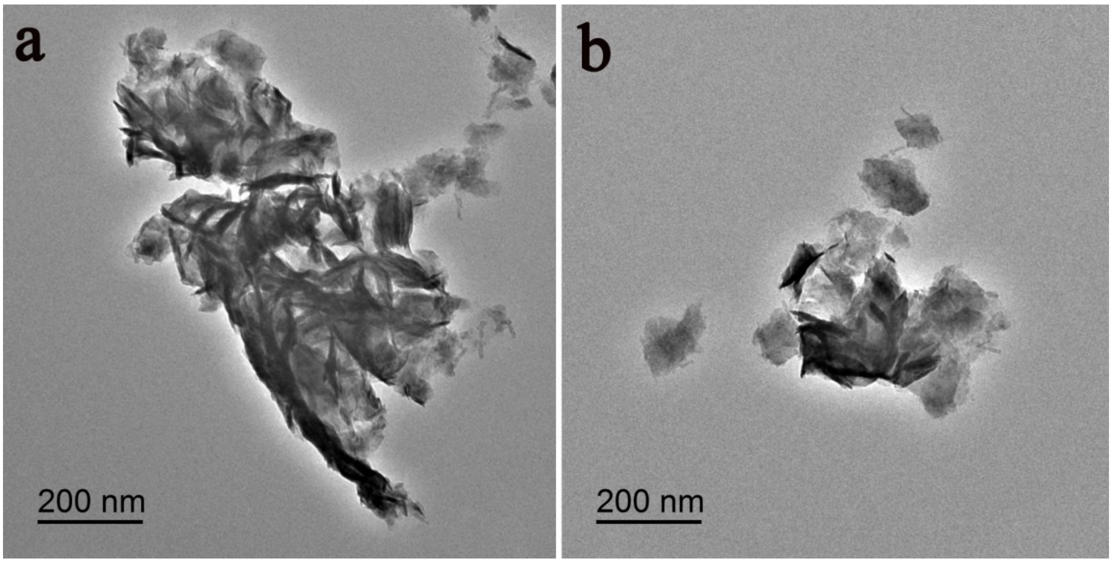

Figure S8 TEM images of (a, b) the pure MoS_2.

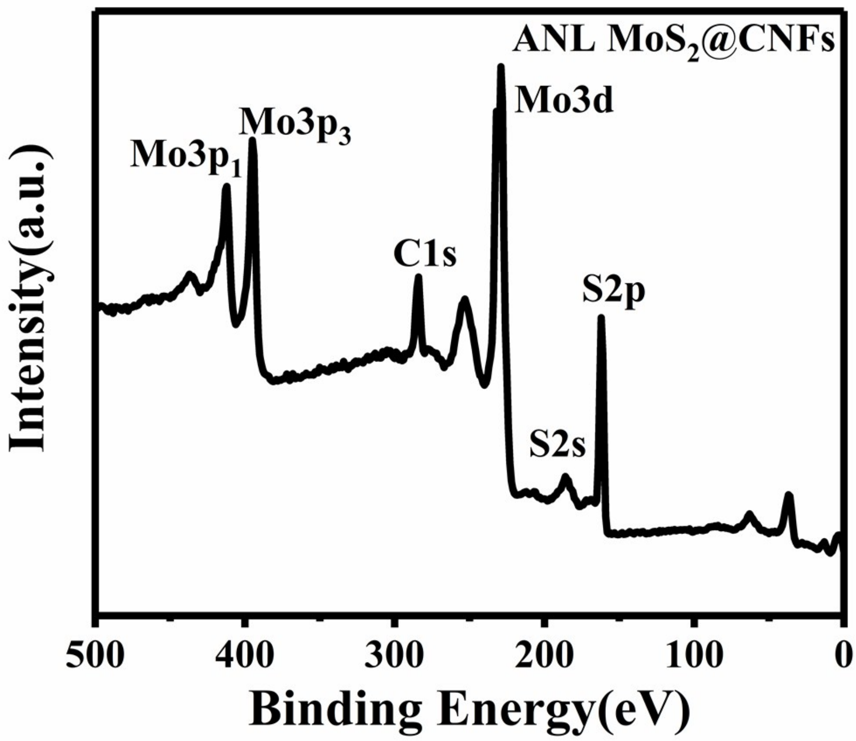

Figure S9 XPS of ANL MoS$_2$@CNFs survey spectrum.

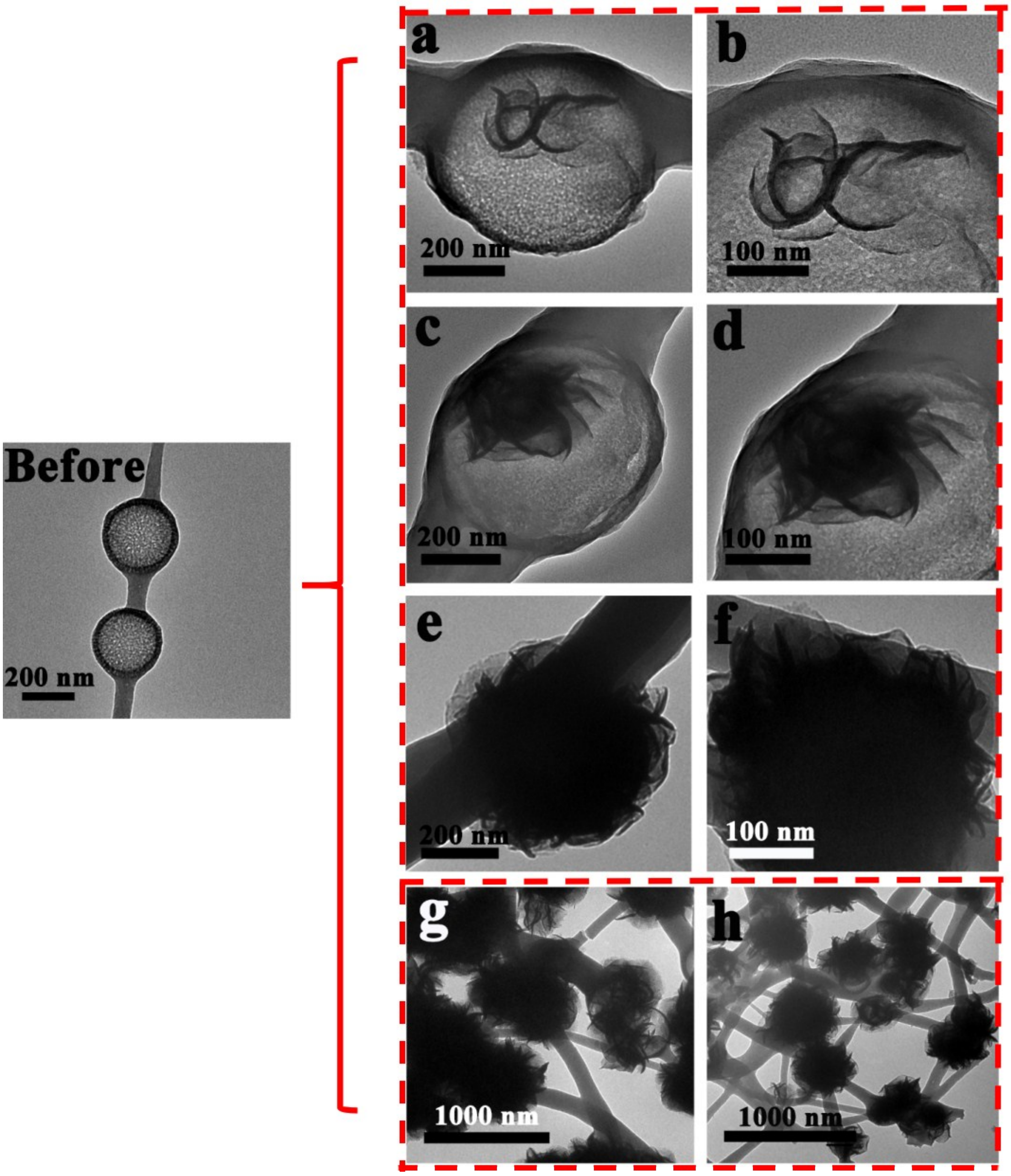

Figure S10 TEM images at different reaction time (a, b) 2 h, (c, d) 4 h and (e, f) 6 h. (g-h) the sample obtained at hydrothermal reaction condition: 1 g $Na_2MoO_4 \cdot 2H_2O$, 2.0 g $CS(NH_2)_2$ and 30 mL deionized water.

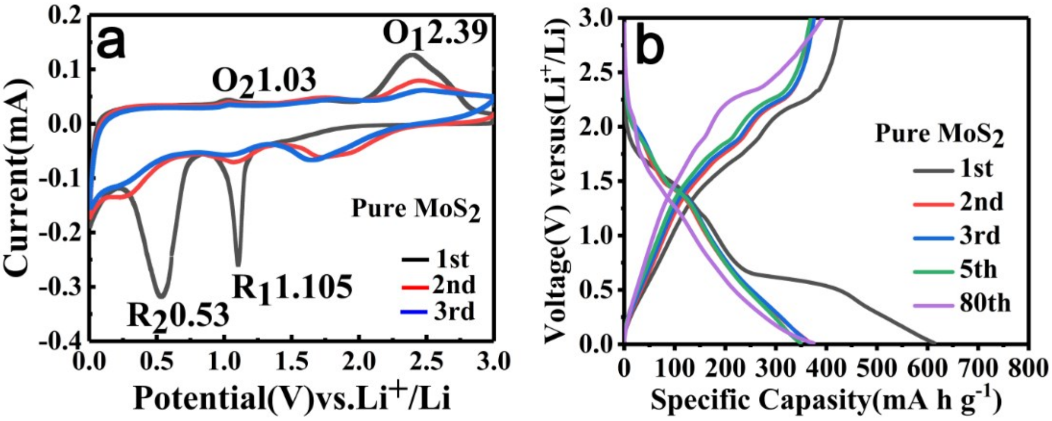

Figure S11 (a) CV and (b) charge/discharge voltage profiles of pure MoS_2.

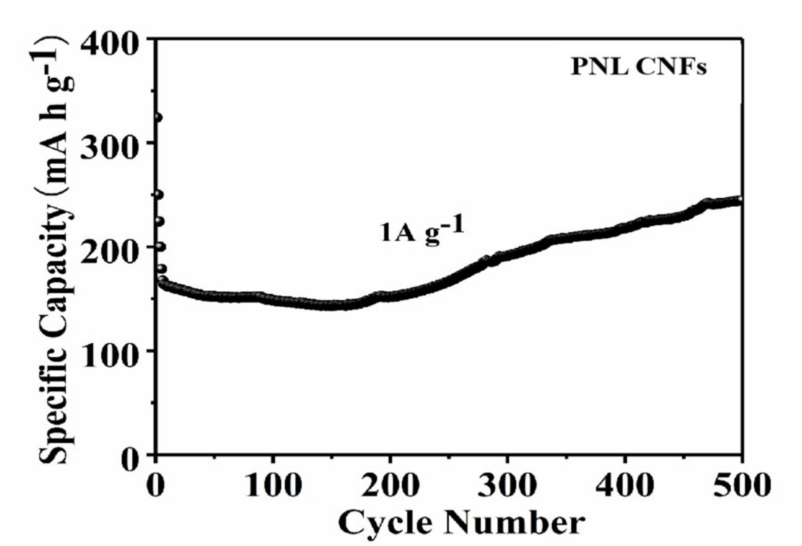

Figure S12 Cycling performance for LIBs of PNL CNFs after 500 cycles at 1 A g^{-1}.

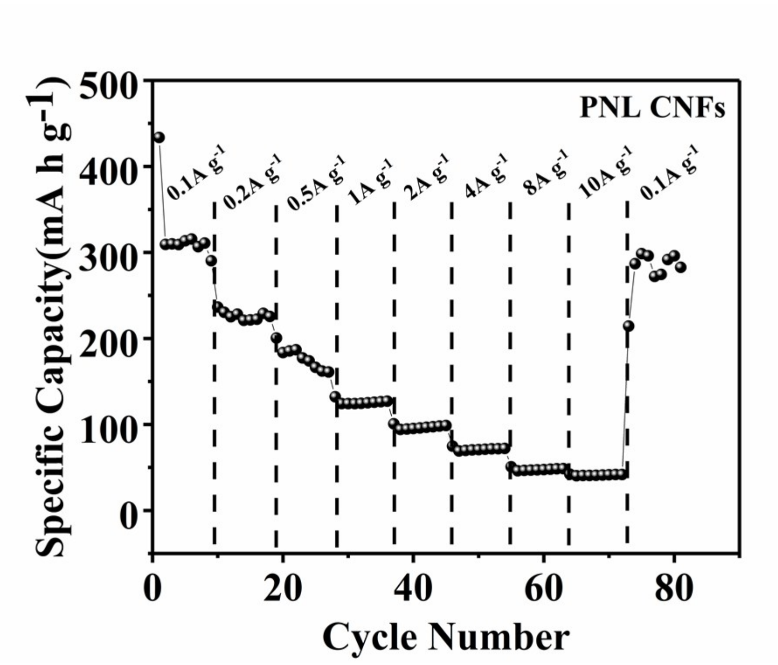

Figure S13 Cycling performance for LIBs of PNL CNFs at various current densities (0.1 to 10 A g^{-1}).

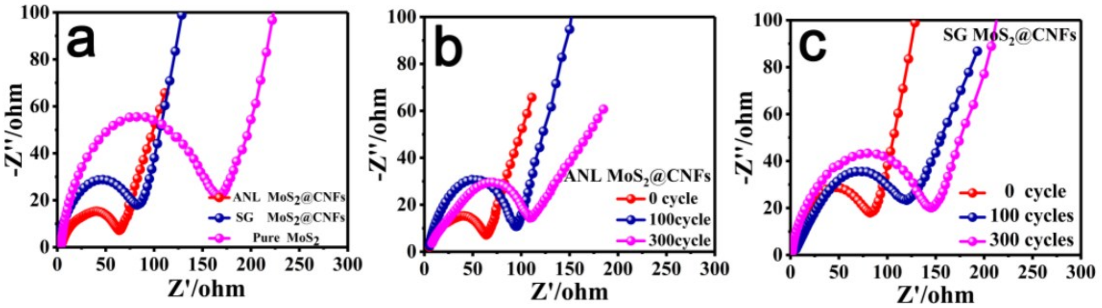

Figure S14 (a) Nyquist plots of ANL MoS_2@CNFs, SG MoS_2@CNFs and pure MoS_2; Nyquist plots of (b) ANL MoS_2@CNFs and (c) SG MoS_2@CNFs after 100 and 300 cycles.

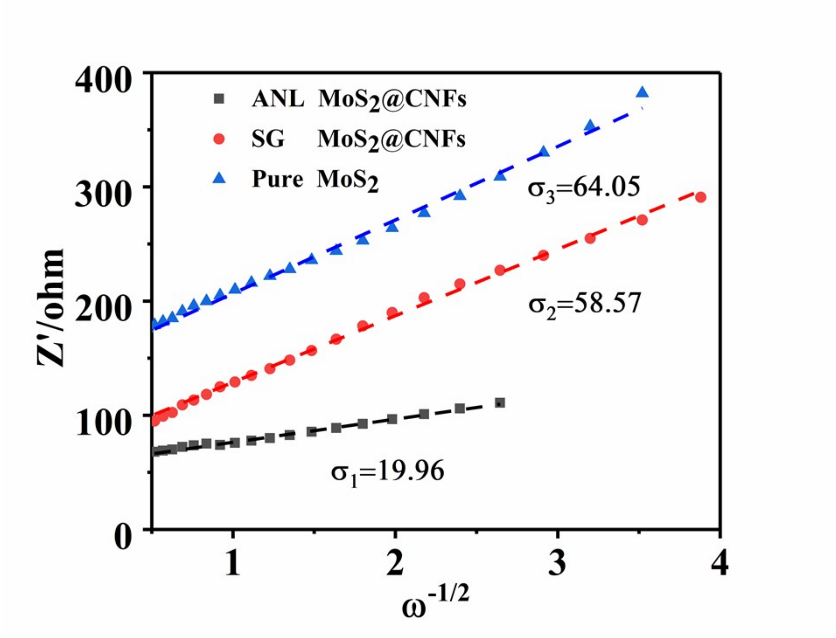

Figure S15 Graph for LIBs of the Z' plotted against $\omega^{-1/2}$ at low frequency region.

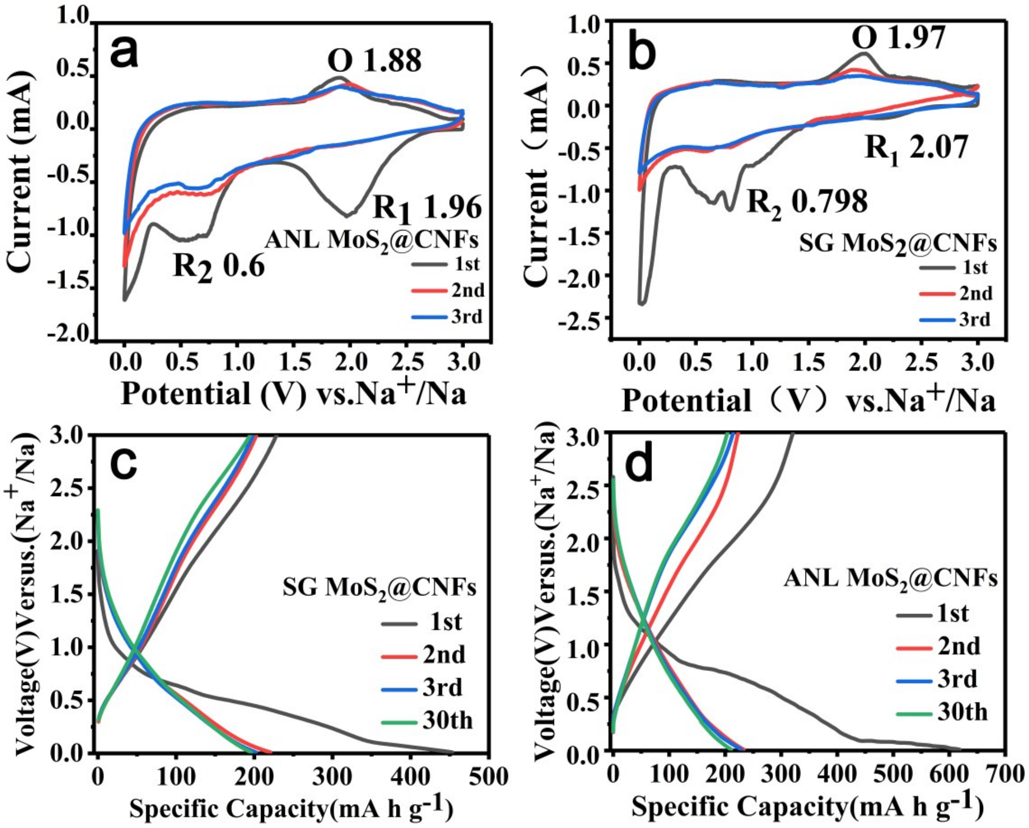

Figure S16 Electrochemical performance for SIBs. CV and charge/discharge voltage profiles of (a, c) ANL MoS_2@CNFs, (b, d) SG MoS_2@CNFs.

Figure S16a shows the first three cycles of ANL MoS_2@CNFs at the sweep rate of 0.1 mV s^{-1}. During the first cathodic scan, the reduction peak at 1.96 V is observed, which indicates the embedding of Na^+ into the MoS_2 nanosheets and the conversion reaction ($MoS_2 + x\ Na^+ + x\ e^- \rightarrow Na_xMoS_2$, $x < 2$). The other peak at 0.6 V corresponds to the formation of Mo metal, Na_2S ($Na_xMoS_2 + (4-x)\ Na^+ + (4-x)\ e^- \rightarrow Mo + 2Na_2S$) and SEI. After the scan of anode part, a wide peak at 1.88 V is observed, which is the reverse conversion reaction between metallic Mo and Na_2S matrix. Besides, the redox peaks of ANL MoS_2@CNFs in the 2nd and 3th cycles are almost coincided, insinuating that the ANL MoS_2@CNFs have outstanding reversibility and stability. However, SG MoS_2@CNFs show poor stability (Figure S16b), the current density begins to decay from the second cycle. At 1 A g^{-1} current density and the voltage range is 0.01-3.0 V versus Na^+/Na, the initial capacities of ANL MoS_2@CNFs are 615 and 322 mA h g^{-1} (Figure S16c), which give an initial CE 52.4% higher than that of SG MoS_2@CNFs (50.5%) (Figure S16d). And the primary irreversible capacity loss is due to the formation of SEI layer. The curves almost coincide with each other after the 1st cycle, suggesting the cyclic stability and outstanding reversibility of the ANL MoS_2@CNFs.

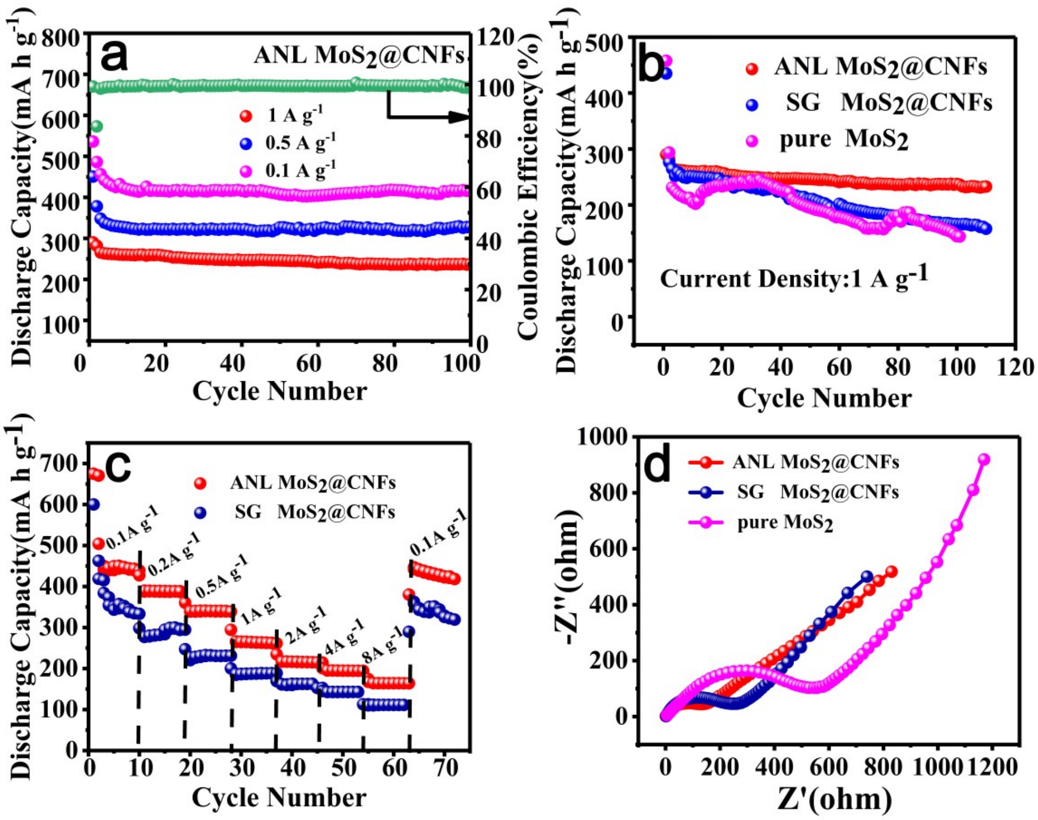

Figure S17 Cycling performance of (a) ANL MoS_2@CNFs at 1, 0.5, 0.1 A g^{-1} and Coulombic efficiency of ANL MoS_2@CNFs at 0.1 A g^{-1}. (b) Cycling performances, (c) rate performances, (d) Nyquist plots of different electrode materials.

In Figure S17a, the ANL MoS_2@CNFs remain excellent cyclic stability and high specific capacities (425 mA h g^{-1}) (nearly 100 % CE) at 0.1 A g^{-1} after 100 cycles. As the rising of current density, the specific capacities of the ANL MoS_2@CNFs begin to reduce, but still maintain good cyclic stability. Moreover, compared the cyclic performance of three electrodes at 1 A g^{-1} (Figure S17b), the ANL MoS^2@CNFs show the best cyclic stability, while the SG MoS_2@CNFs display a tendency of capacity decaying. Because MoS_2 nanosheets are exposed on the surface of the CNFs, the bulk swelling causes the exfoliation from the CNFs, resulting from the capacity attenuation of the SG MoS_2@CNFs.

The rate capacities of the ANL MoS_2@CNFs and SG MoS_2@CNFs electrodes are illustrated at different current densities, as shown in Figure S17c. Relatively, the specific capacities of ANL MoS2@CNFs are 440, 388, 340, 260, 215, 195 and 164 mA h g^{-1}, respectively. Afterwards, as the current density returns to 0.1 A g^{-1}, the specific capacity of ANL MoS_2@CNFs quickly increases to 446 mA h g^{-1}. Evidently, the cyclic performance and the rate property of ANL MoS_2@CNFs are better than those of SG MoS_2@CNFs, pure MoS_2 and PNL CNFs (Figure S18, 19). Finally, compared with other MoS_2-based materials in SIBs listed in Table S3, it is clear that the ANL MoS_2@CNFs is a highly competitive candidate in terms of cycling stability and rate property.

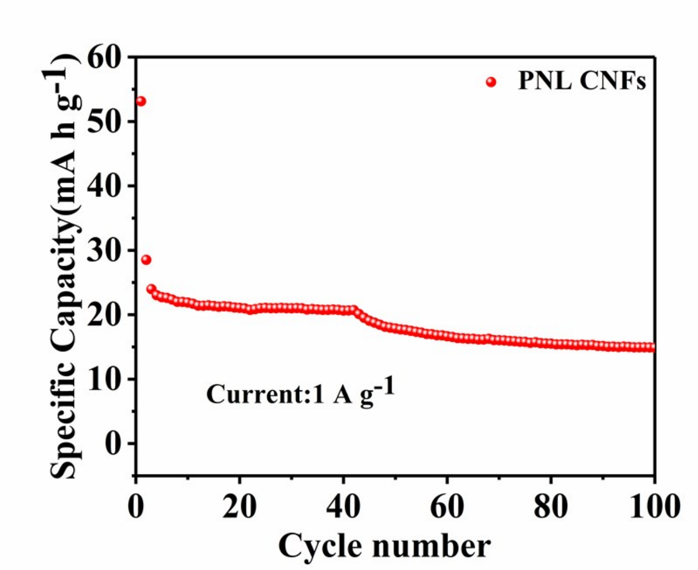

Figure S18 Cycling performance for SIBs of PNL CNFs after 100 cycles at 1 A g^{-1}.

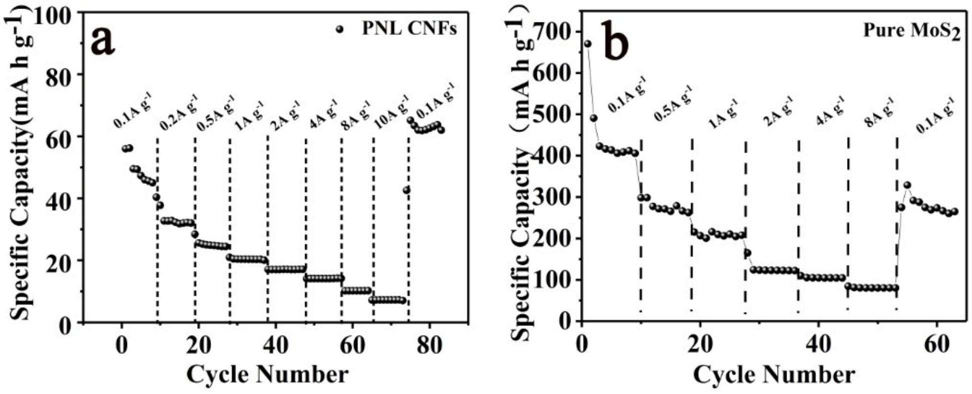

Figure S19 Rate performance for SIBs of PNL CNFs and pure MoS_2 at various current densities.

EIS further confirms the electrochemical reaction kinetics of composites. In Figure S17d, the radius of high-frequency region of ANL MoS_2@CNFs is significantly smaller than those of SG MoS_2@CNFs and pure MoS_2, which indicates that the charge transfer ability of ANL MoS_2@CNFs is superior to others. In addition, the linear slope of the low frequency region of ANL MoS_2@CNFs is much higher than those of SG MoS_2@CNFs and pure MoS_2, implying that sodium ions have the tendency of much easier diffusing in the ANL MoS_2@CNFs electrode. The calculated values of diffusion coefficient (D_{Na^+}) in three materials are shown in Table S4 (more details in Figure S20). Compared with the performance of ANL MoS_2@CNFs in LIBs, the storage sodium performance of ANL MoS_2@CNFs is poor due to large ionic radius and slow migration rate of Na^+.

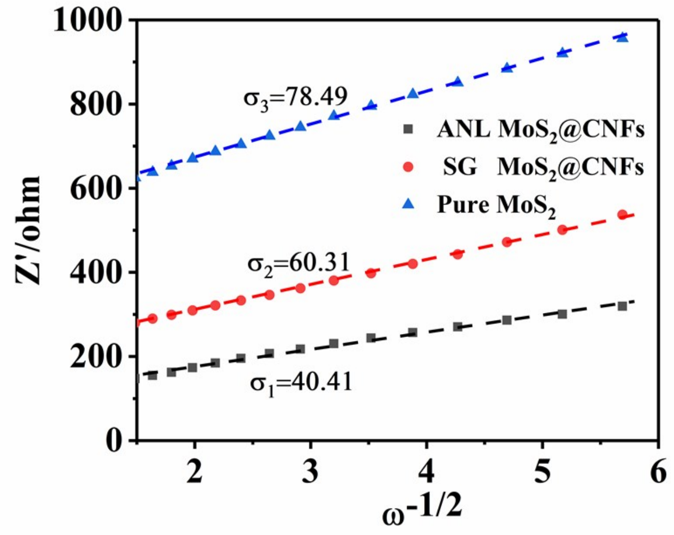

Figure S20 Graph for SIBs of the *Z′* plotted against $\omega^{-1/2}$ at low frequency region.

Table S1 Summary of electrochemical performances of different MoS_2-based anodes for lithium-ion battery.

Sample	**Current density ($A\ g^{-1}$)**	**Initial discharge/charge capacity ($mA\ h\ g^{-1}$)**	**Reversible capacity ($mA\ h\ g^{-1}$)/Cycles/Current density ($A\ g^{-1}$)**	**References**
ANL MoS_2@CNFs	1	1049/802	602/500/1	This work
NDG/MoS2/NDG	0.1	913/770	552/600/1	[1]
Layered C_3N_4/NRGO/MoS_2	0.1	938/722	130/110/8	[2]
MoS_2@CMK-3 Nanocomposite	0.25	1056/824	602/100/0.25	[3]
Core-shell MoS_2	0.1	850/550	690/100/0.1	[4]
Quasi-hollow C@MoS_2	0.1	857/566	652/100/0.1	[5]

Table S2 R_{ct}, σ and D_{Li} of ANL $\mathrm{MoS_2}$@CNFs, SG $\mathrm{MoS_2}$@CNFs and Pure $\mathrm{MoS_2}$.

Samples	**R_{ct}/Ω**	**σ**	**$D_{\mathrm{Li}}/\mathrm{cm^2\ s^{-1}}$**
ANL $\mathrm{MoS_2}$@CNFs	63.9	19.96	7.23×10^{-14}
SG $\mathrm{MoS_2}$@CNFs	82.2	58.57	8.40×10^{-15}
Pure $\mathrm{MoS_2}$	166.5	64.05	7.02×10^{-15}

The following equation can be used to calculate the diffusion coefficient of the $\mathrm{Li^+}$ (D_{Li}) (1)

$$D_{\mathrm{Li}} = \frac{R^2T^2}{2A^2n^4F^4c^2\sigma^2} \tag{1}$$

Here, R is the gas constant, T *is* the absolute temperature, A is the electrode area, n represents the electrons number, F is the Faraday constant, c is the lithium ion concentration, and σ shows the Warburg factor, which relates to Z' through equation $Z' = R_s + R_{ct} + \sigma\omega^{-1/2}$. The σ can be obtained from the slope of Figure S15.

Table S3 Summary of electrochemical performances of different MoS_2-based anodes for sodium-ion battery.

Sample	**Current density (A g^{-1})**	**Initial discharge/charge capacity (mA h g^{-1})**	**Reversible capacity (mA h g^{-1})/ Cycles/Current density (A g^{-1})**	**References**
ANL MoS_2@CNFs	1	615/322	425/100/0.1 260/100/1	This work
MoS_2@C-CMC	0.08	450/350	286/100/0.08	[6]
MoS_2/graphene	0.025	943/347	230/20/0.025	[7]
MoS_2/CNTs	0.05	920/604	504.6/100/0.05	[8]
MoS_2/C	0.07	1500/671	520/50/0.07	[9]
Exfoliated MoS_2 Nanosheets	0.04	998/420	251/100/0.32	[10]

Table S4 R_{ct}, σ and D_{Na} of ANL MoS_2@CNFs, SG MoS_2@CNFs and pure MoS_2.

Samples	R_{ct}/Ω	σ	D_{Na}/cm^2 s^{-1}
ANL MoS_2@CNFs	132	40.41	1.76×10^{-14}
SG MoS_2@CNFs	245	60.31	7.92×10^{-15}
Pure MoS_2	529	78.49	4.67×10^{-15}

The diffusion coefficient D of the diffusion of sodium ions inside the solid particulate material can be calculated by Equation (2)

$$D = \left(\frac{RT}{\sqrt{2}\mathrm{n}^2 F^2 \sigma A C} \right)^2 \tag{2}$$

Here, R is the gas constant, T *is* the absolute temperature, A is the electrode area, n represents the electrons number, F is the Faraday constant, C is the sodium ion concentration, and σ shows the Warburg factor, which relates to Z' through equation $Z' = R_s + R_{SEI} + R_{ct} + \sigma\omega^{-1/2}$. The σ can be obtained from the slope of Figure S20.

Reference

1. Chen, B.; Meng, Y.; He, F.; Liu, E.; Shi, C.; He, C.; Ma, L.; Li, Q.; Li, J.; Zhao, N., Thermal decomposition-reduced layer-by-layer nitrogen-doped graphene/MoS_2/nitrogen-doped graphene heterostructure for promising lithium-ion batteries. *Nano Energy.* **2017**, 41, 154-163.
2. Hou, Y.; Li, J.; Wen, Z.; Cui, S.; Yuan, C., Chen, J., N-doped graphene/porous g-C_3N_4 nanosheets supported layered-MoS_2 hybrid as robust anode materials for lithium-ion batteries. *Nano Energy.* **2014**, 8, 157-164.
3. Zhou, X.; Wan, L. J.; Guo, Y. G., Facile synthesis of MoS_2@CMK-3 nanocomposite as an improved anode material for lithium-ion batteries. *Nanoscale.* **2012**, 4, 5868-71.
4. Wan, Z.; Shao, J.; Yun, J.; Zheng, H.; Gao, T.; Shen, M.; Qu, Q.; Zheng, H., Core-Shell Structure of Hierarchical Quasi-Hollow MoS_2 Microspheres Encapsulated Porous Carbon as Stable Anode for Li-Ion Batteries. *Small.* **2014**, 10, 4975-4981.
5. Sun, Z.; Yao, Y.; Wang, J.; Song, X.; Zhang, P.; Zhao, L.; Gao, L., High rate lithium-ion batteries from hybrid hollow spheres with a few-layered MoS_2-entrapped carbon sheath synthesized by a space-confined reaction. *Journal of Materials Chemistry A.* **2016**, 4, 10425-10434.
6. Xie, X.; Makaryan, T.; Zhao, M.; Van Aken, K. L.; Gogotsi, Y.; Wang, G., MoS_2 Nanosheets Vertically Aligned on Carbon Paper: A Freestanding Electrode for Highly Reversible Sodium-Ion Batteries. *Advanced Energy Materials.* **2016**, 6, 1502161.

7. David, L.; Bhandavat, R.; Singh, G., MoS_2/graphene composite paper for sodium-ion battery electrodes. *ACS nano.* **2014**, 8, 1759-70.

8. Zhang, S.; Yu, X.; Yu, H.; Chen, Y.; Gao, P.; Li, C.; Zhu, C., Growth of ultrathin MoS_2 nanosheets with expanded spacing of (002) plane on carbon nanotubes for high-performance sodium-ion battery anodes. *ACS applied materials & interfaces.* **2014**, 6, 21880-5.

9. Wang, J.; Luo, C.; Gao, T.; Langrock, A.; Mignerey, A. C.; Wang, C., An advanced MoS_2/carbon anode for high-performance sodium-ion batteries. *Small.* **2015**, 11, 473-81.

10. Su, D.; Dou, S.; Wang, G., Ultrathin MoS_2 Nanosheets as Anode Materials for Sodium-Ion Batteries with Superior Performance. *Advanced Energy Materials.* **2015**, 5, 1401205.